Influence of Loading Conditions in Finite Element Analysis Assessed by HR-pQCT on Ex Vivo Fracture Prediction

Martin Revel, François Bermond, Francois Duboeuf, David Mitton, Hélène Follet

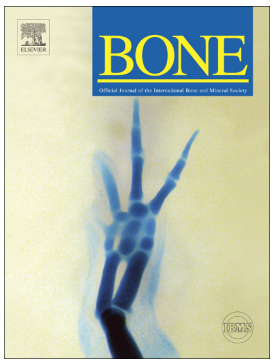

Influence of Loading Conditions in Finite Element Analysis Assessed by HR–pQCT on Ex Vivo Fracture Prediction

M. Revel, F. Bermond, F. Duboeuf, D. Mitton, H. Follet

PII: S8756-3282(21)00372-0

DOI: https://doi.org/10.1016/j.bone.2021.116206

Reference: BON 116206

To appear in: *Bone*

Received date: 19 April 2021

Revised date: 15 September 2021

Accepted date: 15 September 2021

Please cite this article as: M. Revel, F. Bermond, F. Duboeuf, et al., Influence of Loading Conditions in Finite Element Analysis Assessed by HR–pQCT on Ex Vivo Fracture Prediction, *Bone* (2021), https://doi.org/10.1016/j.bone.2021.116206

Influence of Loading Conditions in Finite Element Analysis Assessed by HR–pQCT on *Ex Vivo* Fracture Prediction.

M. Revel [1, 2], F. Bermond [2], F. Duboeuf[1], D. Mitton [2], H. Follet [1]

[1] Univ Lyon, Univ Claude Bernard Lyon 1, INSERM, LYOS UMR1033, F69008, Lyon, France

[2] Univ Lyon, Univ Gustave Eiffel, Univ Claude Bernard Lyon 1, LBMC UMR_T9406, F69622, Lyon, France

***Corresponding author**:*

Hélène Follet

Univ Lyon – INSERM, UMR1033

Faculté de Médecine Lyon Est –Domaine Laennec–6th

7–11, rue G. Paradin

69372 Lyon cedex 08

France

Phone: +33 4 78 78 57 26

E–mail address: helene.follet@inserm.fr

Keywords: Forward Fall, HR–pQCT, Fracture Prediction, Radius, Bone strength

Abstract

Many fractures occur in individuals with normal areal Bone Mineral Density (aBMD) measured by Dual X–ray Absorptiometry (DXA). High Resolution peripheral Quantitative Computed Tomography (HR–pQCT) allows for non–invasive evaluation of bone stiffness and strength through micro finite element (μFE) analysis at the tibia and radius. These μFE outcomes are strongly associated with fragility fractures but do not provide clear enhancement compared with DXA measurements. The objective of this study was to establish whether a change in loading conditions in standard μFE analysis assessed by HR–pQCT enhance the discrimination of low-trauma fractured radii (n = 11) from non-fractured radii (n = 16) obtained experimentally throughout a mechanical test reproducing a forward fall. Micro finite element models were created using HR–pQCT images, and linear analyses were performed using four different types of loading conditions (axial, non-axial with two orientations and torsion). No significant differences were found between the failure load assessed with the axial and non–axial models. The different loading conditions tested presented the same area under the receiver operating characteristic (ROC) curves of 0.79 when classifying radius fractures with an accuracy of 81.5%. In comparison, the area under the curve (AUC) is 0.77 from DXA-derived ultra-distal aBMD of the forearm with an accuracy of 85.2%. These results suggest that the restricted HR–pQCT scanned region seems not sensitive to loading conditions for the prediction of radius fracture risk based on *ex vivo* experiments (n = 27).

1 Introduction

Mobility may be affected by age–related pathologies, such as osteoporosis with a consequent increase in bone fragility and susceptibility to fracture, which is expected to increase in the next two decades given the elderly population growth. Nowadays, osteoporosis remains underdiagnosed and undertreated [1,2].

The current standard method for clinical diagnosis of osteoporosis and evaluation of fracture risk is Dual X–ray Absorptiometry (DXA) combined with assessment of clinical risk factors with the Fracture Risk Assessment Tool (FRAX), which predicts 10–year fracture risk [3]. This method is based on measurements of areal Bone Mineral Density (aBMD) at different anatomical sites. However, this measure presents insufficient sensitivity with 50% of fragility fractures occurring in patients considered non-osteoporotic [4]. Hence, another technique as High Resolution peripheral Quantitative Computed Tomography (HR–pQCT), was introduced in the mid–2000's. This device allows non-invasive evaluation of three-dimensional microarchitecture and bone strength at the tibia and radius [5]. HR–pQCT offers significant advantages over the measurement of aBMD. In addition to volumetric Bone Mineral Density (vBMD), HR–pQCT provides assessment of bone structure of a segment of 9.02 mm of bone through high–resolution 3D images with an isotropic resolution of 82 $\mu m \times 82\ \mu m \times 82\ \mu m$ as well as bone stiffness and strength through micro finite element (μFE) analysis [6–8].

This approach, based on structural mechanics, showed that μFE analyses better predict forearm bone strength (R^2 between 0.73 and 0.92) than DXA measurements (R^2 between 0.31 and 0.71) [9]. But, despite this good level of prediction, no retrospective [6,10–14] or

prospective [15–17] cohort study established better prediction of the fracture risk with these μFE analysis compared with the standard reference method, although it is doing clearly at least as well as the DXA. It is only with the Bone Micro architecture International Consortium (BoMIC), which includes participants of eight cohorts, that μFE outcomes improved prediction of incident fracture beyond femoral neck aBMD and FRAX with higher hazard ratios [18]. Nevertheless, even if models that combines μFE and femoral neck aBMD improved the ability to predict non-traumatic or traumatic incident fracture, this was not the case when considering only major osteoporotic fractures [18].

Nevertheless, μFE is associated with incident fracture independently of femoral neck DXA, BMD, and FRAX [18]. Changing certain numerical parameters (loading conditions, scan length, resolution...) are potential ways to improve finite element modeling and deserves particular attention for the improvement of fracture prediction. Considering that forearm fractures were almost exclusively caused by a fall from a standing height in a forward direction [18–20] and that boundary conditions have a large effect on radius fracture load in continuum finite element models [21,22] loading orientation should be considered as a non-axial impact on the wrist, which differs from the axial compression utilized in HR–pQCT μFE analysis.

In this context, the objective of this study is to compare the axial compression currently used with other loading modes to discriminate fractured radius from non-fractured radius obtained in a previous *ex vivo* experimental study reproducing a forward fall under dynamic loading conditions [23].

2 Materials and Methods

2.1 Specimens and image acquisition

Thirty fresh–frozen cadaveric left radii from elderly donors (50–96 y.o., 79±12 y.o., 15 males, 15 females) provided by the University Department of Anatomy Rockefeller (Lyon, France) were considered for this study (French Ministry of Education and Research, authorization n°DC–2015–2357). The forearms were dissected and two–third of the distal radii were extracted and cleaned of soft tissues. Each radius was wrapped in a saline–moistened gauze and stored frozen at –20°C between the steps of the scanning and mechanical tests. After being thawed at room temperature, the sample collection was scanned using the HR–pQCT device (XtremeCT I, Scanco Medical, Switzerland), with an 82 µm isotropic spatial resolution, according to the manufacturer's standard *in vivo* acquisition protocol (60 kVp, 900 mA, matrix size of 1536 x 1536) [5]. The volume of interest thus scanned corresponds to a 9.02 mm thick (110 slices) region located 9.5 mm proximal to the endplate landmark. After semi–automatic separation of the cortical from the trabecular bone using dual threshold technique, segmentation of the 3D reconstruction was performed with a Laplace–Hamming filter available in XtremeCT software before applying a fixed threshold of 400/1000 of the maximal grayscale value to isolate bone tissue from marrow. This fixed threshold was determined so that the structural indices calculated by HR–pQCT correspond best with those obtained from µCT images with a resolution of 28 µm [24]. Moreover, areal Bone Mineral Density (aBMD, g/cm^2) and Bone Mineral Content (BMC, g) were measured using Dual X–ray Absorptiometry (DXA, Hologic, USA) for each frozen bone in the proximal (1/3), middle (MID), and ultra-distal (UD) regions, and the T–scores were retrieved.

2.2 *Ex–vivo* experiment

As described in a previous study in more detail [23], an experimental protocol of forward fall on the radius was performed on the 30 specimens in order to distinguish two groups: the fractured bones from the non-fractured bones. The radii were potted in polyurethane resin in a hollow steel cylinder, with an angle of 75±2° between the anterior face of the radius and the impactor. This position reproduces the most common alignment of the radius during a forward fall [25]. Because carpal bone, particularly the scaphoid and lunatum, were involved in the fracture mechanism [21,26], a rigid polyurethane mold was created to reproduce a simplification of this joint and evenly distribute the load on the articular surface of the radius throughout the impact. In summary, a shell of modeling clay was made surrounding the distal radius, and liquid silicone was sprayed over the articular surface. A polyurethane resin was then poured; after polymerization, the shell of modelling clay was removed. During the test, the mold was maintained with silicone rubber. The specimens were then placed in a horizontal cylinder bar on a rail system, which is free to slide along the loading axis. This bar has a weight of 12.5 kg, which is an arbitrary value representing the mass involved in a fall (i.e., a percentage of body weight). Each radius was then loaded with a unique velocity of 2 m/s using a hydraulic high–speed testing machine (LF Technologies, France) (Fig. 1).

A six–axis sensor (105515TF, Humanetics, Germany) was tightened onto the impactor in order to obtain the reaction load curve over time and to retrieve the maximum load of each specimen during the impact. Four high–speed cameras (FASTCAM SA3, Photron, Japan) placed in pairs facing the ulnar surface of the radius and facing the anterior surface of the radius recorded the impact with a resolution of 1024 x 1024 pixels at 2000 frames per

second with a shutter speed of 50 µs. Bone fracture was assessed by using the high–speed recordings; then, a radiologist interpreted the radiographs after the impact. These experiments were used to obtain known status of bone fractures for the numerical sensitivity/specificity study.

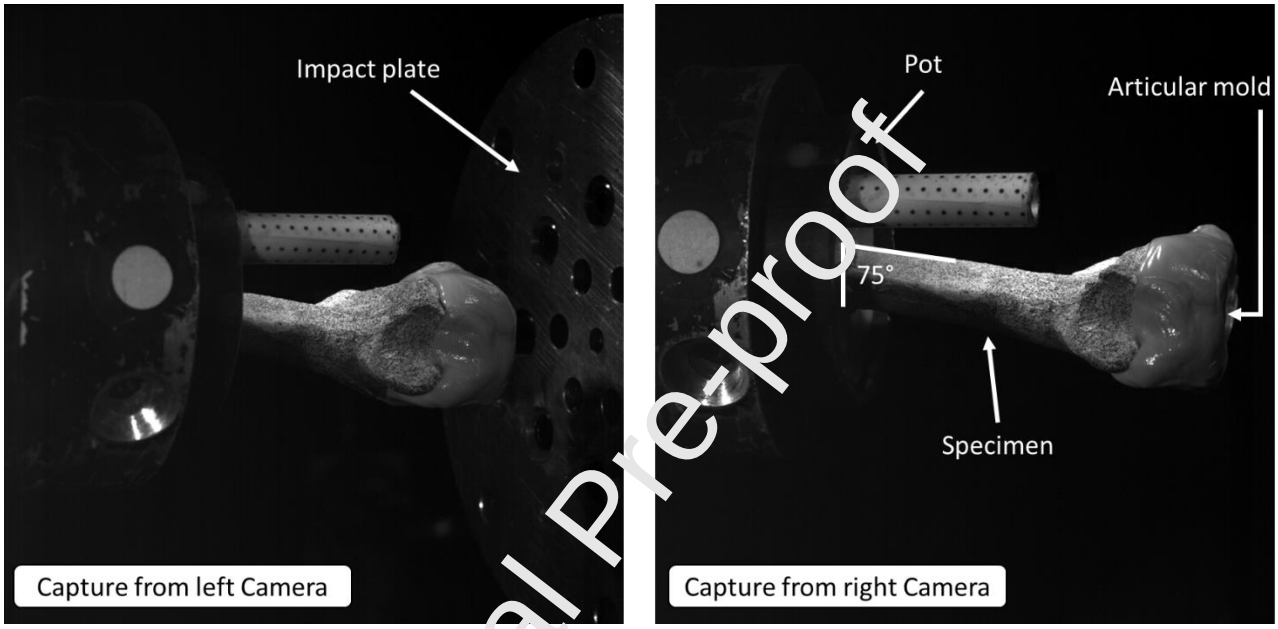

Figure 1: Setup of the experiment captured from the high–frequency lateral cameras. The specimen oriented at 75 ° is impacted to the ground at 2m/s through the articular mold in polyurethane resin (maintained with silicone rubber).

2.3 µFE Model

Finite element models of the 9.02 mm length of radius were generated directly from the segmented HR–pQCT images using software delivered by the manufacturer (IPL FE, Scanco Medical) with a voxel–conversion method. Each voxel of bone tissue was converted to an 8–nodes linear hexahedral element with reduced integration and leads to models with a total number of elements varying from 0.75 to 3.5 million (mean, 2.02±0.75 millions) after deletion of the elements or groups of elements isolated from the main structure (Fig. 2).

Finally, the µFE models were rotated along their longitudinal axis to orient each anterior face of the bone, as a geometric reference, in the same direction for all samples and exported to be usable in Ansys finite element software (v2019R1, Ansys® Inc., USA).

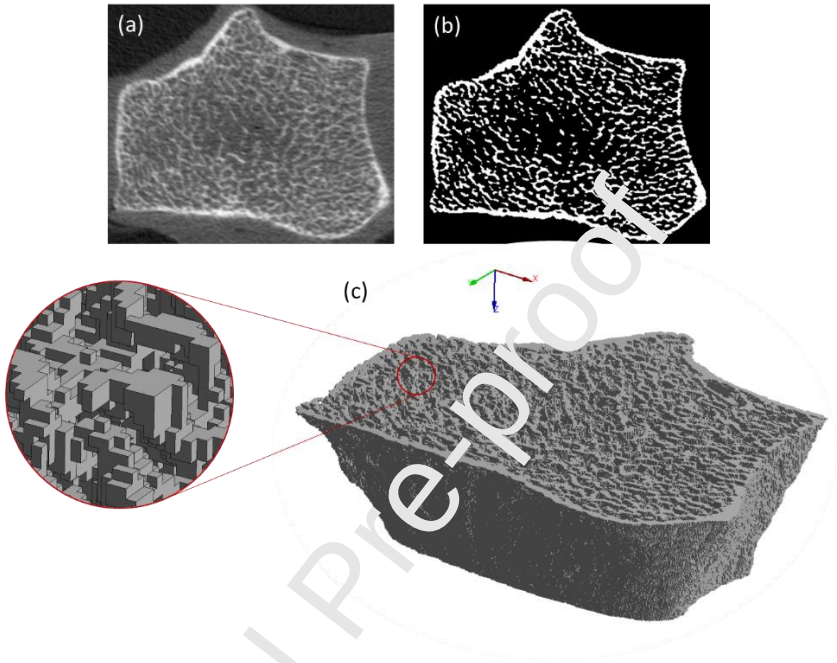

Figure 2: The different stages of model creation. (a) Initial grayscale image (transverse view) (b) Segmented image after filtering and thresholding (c) Mesh generated by voxel conversion composed of millions of hexahedral elements. The longitudinal axis corresponds to the z axis in (blue), the anterior face of the bone faces the y axis (in green).

Despite the discrepancies in the literature for material properties [6,27–29], harmonization methods exist for the first–generation HR–pQCT to compare results across studies [30]. Material properties were then assumed to be homogeneous, linear elastic, and isotropic with an assigned Young's modulus of 10 GPa and a Poisson's ratio of 0.3 [7].

In vivo, the complexity of loadings is not known for specific patients, thus the choice in the current study was to consider four arbitrary types of boundary conditions. For all loadings,

the nodes of the most proximal plane were fully constrained. The first case was the standard HR–pQCT axial compression test, where an arbitrary displacement of 1% of the segment thickness was applied to the nodes of the most distal plane with their in–plane motion constrained [6,14,31]. The second and third cases considered non-axial loading. The displacement vector was multiplied by the rotation matrix:

$$R_x(\theta) = \begin{pmatrix} 1 & 0 & 0 \\ 0 & \sin\theta & -\cos\theta \\ 0 & \cos\theta & \sin\theta \end{pmatrix}$$

where θ is the angle between the longitudinal axis of the model and the floor (Fig. 3). Two orientations were investigated : a displacement of 75° and 45° to assess the influence of the angle on the numerical response.

Figure 3: Positioning and orientation of the 9.02 mm segment during a forward fall

The fourth case considered a pure torsional loading to assess the influence of an atypical loading. An arbitrary rotation of 1° was applied to the nodes in the distal plane. These boundary conditions are summarized in Figure 4. Linear analyses of the models were performed using Ansys software (v2019R1, Ansys® Inc., USA) with a 20 cores CPU with a clock frequency of 2.40 GHz and 64 GB RAM.

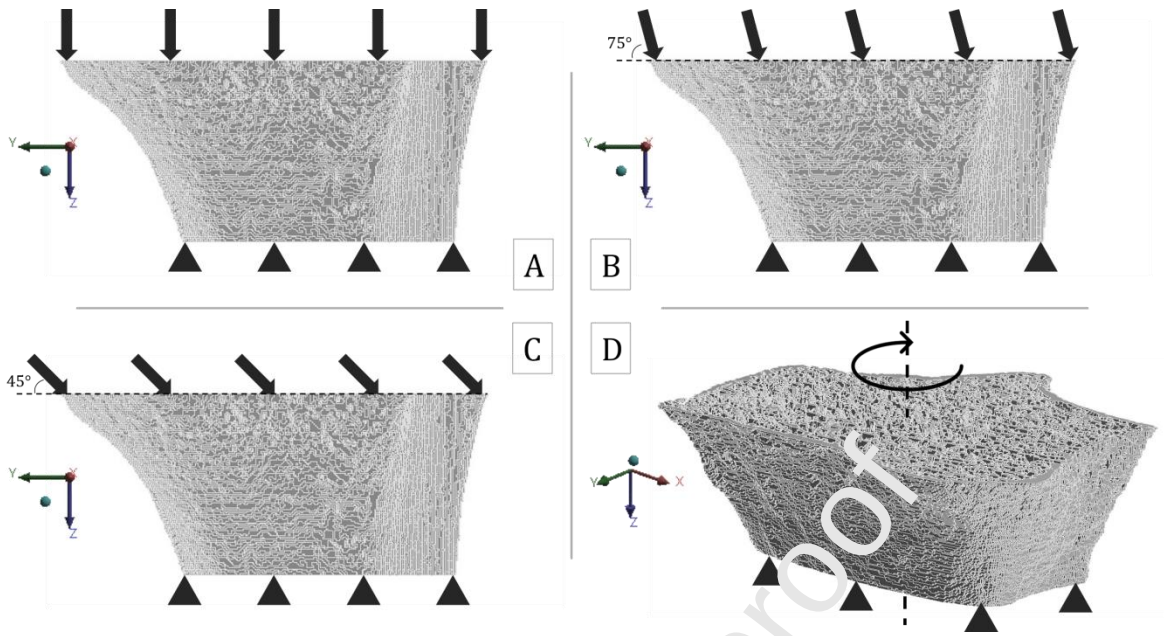

Figure 4: Boundary conditions used with in: (A) The axial standard compression with in–plane motion constrained, (B) the 75° off–axis loading with motion in the x direction constrained, (C) the 45° off–axis loading with motion in the x direction constrained and (D) the torsional loading.

The total reaction force and torque magnitude of the numerical tests were exported. Failure loads and torque were estimated with two failure criteria. The validated and standarized Pistoia's criterion [7,30,32] and the Mohr–Coulomb's theory which described the response of brittle materials to shear stress as well as normal stress [21,26] (Table 1). Failure occurred when a criterion is greater than or equal to 1 for 2% of the elements. The compressive failure strain (ε_{yc}) was set to 0.7% [7]. The compressive failure strength (σ_{yc}) was determined by multiplying ε_{yc} by the Young's modulus E, assuming the tensile failure strength $\sigma_{yt} = 0.5 \times \sigma_{yc}$ [21,26].

Table 1: The failure criterion investigated with their respective equations. $\boldsymbol{\varepsilon_{eff}}$ is the effective strain estimated from the strain energy density [7] and $\boldsymbol{\sigma_1}$, $\boldsymbol{\sigma_2}$, and $\boldsymbol{\sigma_3}$ are the principal stresses ($\boldsymbol{\sigma_1 > \sigma_2 > \sigma_3}$).

Criterion	Equation
Pistoia's Criterion	$\frac{\varepsilon_{eff}}{\varepsilon_{yc}} \geq 1$
Mohr–Coulomb's (MC) Criterion	$\frac{\sigma_1}{\sigma_{yt}} - \frac{\sigma_3}{\sigma_{yc}} \geq 1$

2.4 Statistical Analysis

Gaussian distribution of the parameters were assessed using a Shapiro–Wilk's test. Non-parametric statistical tests were considered. First, Spearman's correlation tests were performed between the results based on the different load cases and failure criteria. Then, the medians, min, and max of each output parameter of the numerical simulations were calculated, and the difference in position of the samples between the groups (*i.e.,* the population difference between the groups) of fractured or unfractured bones was evaluated using an unpaired Mann–Whitney U test. The small number of samples in each of the sexes did not allow us to separate males from females in the fracture discrimination analysis, even if significant differences were found between sexes. Nevertheless, a sensitivity/specificity analysis was performed by plotting Receiver Operating Characteristics curves (ROC curves) with their area under the curve (AUC) to determine the optimal threshold for each outcome. This optimal threshold was defined as the point of the curve farthest from the diagonal corresponding to the maximum of the sensitivity + specificity index. For each optimal detection threshold, the test accuracy was calculated as the ratio of true positives (TP) and true negatives (TN) divided by the number of samples ($\frac{TP+TN}{n}$). In order to adjust the p–value of our multiple comparisons, the significance level

was lowered to 0.026 or less after Holm–Bonferroni correction [33]. All the tests were carried out using R software (R Foundation for Statistical Computing, Austria).

3 Results

Among the 30 radii, the experiments failed for two specimens due to misalignments of the potted bones, and the fracture was uncertain for an additional specimen. Finally, 27 bones were tested successfully. As described in the previous study [23], 11 had fractures (7 women, 4 men) after impact and 16 did not fracture (5 women, 11 men). The age of the samples with fractures (median [min–max]: 78 [50–98] years) did not differ significantly from those without fractures (83 [57–96] years), sex pooled (p=0.66). In contrast, although fractures were not consistently associated with weaker reaction forces, a significant difference was found between the two groups (fractured: 2.38 [1.18–3.83]kN, unfractured: 3.8 [1.69–6.27]kN, Difference: –37.3%, p<0.01) regardless of gender.

Table 2 summarizes Spearman's correlation coefficients between all investigated load cases and failure criteria. The compression tests showed strong correlation (ρ>0.98) with a highly linear relationship among the axial, 75°, and 45° load cases (Figure 5). Failure torque remains strongly correlated with the compression failure load but with a lower coefficient (ρ=0.933).

Table 2: Spearman's coefficients ρ between the results based on the different load cases and failure criteria. Values in bold are results with a p–value < 0.0001

Parameters	Pistoia's Criterion				Mohr–Coulomb's Criterion			
	Failure Load Axial	Failure Load 75	Failure Load 45	Failure Torque	Failure Load Axial	Failure Load 45	Failure Load 75	Failure Torque
Pistoia's Criterion								
Failure Load – axial	1	**0.997**	**0.986**	**0.933**	**0.999**	**0.982**	**0.996**	**0.936**
Failure Load – 75°	–	1	**0.993**	**0.937**	**0.996**	**0.990**	**0.997**	**0.939**
Failure Load – 45°	–		1	**0.940**	**0.994**	**0.996**	**0.990**	**0.941**
Failure Torque	–	–	–	1	**0.929**	**0.932**	**0.926**	**0.999**
Mohr–Coulomb's Criterion								
Failure Load – axial	–	–	–	–	1	**0.980**	**0.996**	**0.933**
Failure Load – 75°	–	–	–	–	–	1	**0.990**	**0.934**
Failure Load – 45°	–	–	–	–	–	–	1	**0.929**
Failure Torque	–	–	–	–	–	–	–	1

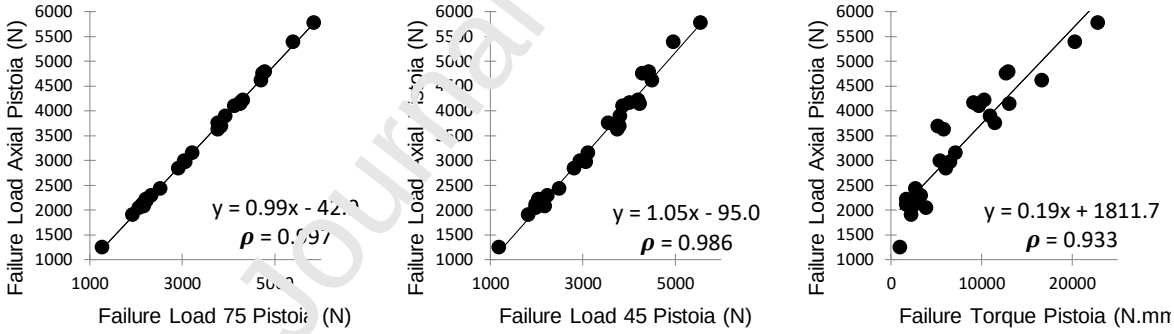

Figure 5 : Scatter plot between Axial failure load and the different loading conditions with their spearman's ρ squared correlation coefficients and linear relationships

The median, minimum, and maximum of the μFE results with the difference between the groups as well as the significance of the Mann–Whitney test are summarized in Table 3. The mechanical parameters evaluated by μFE were strongly associated with fractures showing a significantly lower compressive bone strength of approximatively 43% for fractured bones compared with unfractured bones ($p<0.01$) for any failure criteria as well as ultimate torque of 71% lower ($p=0.01$).

Table 3: Median [Min – Max] of the numerical outcomes among the two fracture groups. The difference between the groups (fractured vs unfractured) is given as a percentage relative to the values of the unfractured with a significance corresponding to the Mann–Whitney U test.

Parameters	Unfractured (n = 16)	Fractured (n = 11)	Difference (%)	p–value
DXA Distal aBMD (g/cm^2)	0.42 [0.28 – 0.52]	0.30 [0.16 – 0.51]	–28.7	0.02
Pistoia's Criterion				
Failure Load (kN) – axial	3.82 [2.15 – 5.77]	2.18 [1.25 – 4.78]	–42.9	<0.01
Failure Load (kN) – 75°	3.89 [2.19 – 5.85]	2.22 [1.26 – 4.79]	–42.8	0.01
Failure Load (kN) – 45°	3.80 [2.04 – 5.55]	2.18 [1.19 – 4.43]	–42.7	0.01
Failure Torque (kN.mm)	9.24 [1.73 – 22.85]	2.74 [1.02 – 12.96]	–71.0	0.01
Mohr–Coulomb's Criterion				
Failure Load (kN) – axial	3.64 [2.04 – 5.63]	2.05 [1.17 – 4.58]	–43.7	<0.01
Failure Load (kN) – 75°	3.74 [2.09 – 5.61]	2.08 [1.21 – 4.65]	–44.3	<0.01
Failure Load (kN) – 45°	3.58 [1.91 – 5.17]	2.03 [1.10 – 4.20]	–43.4	0.01
Failure Torque (kN.mm)	8.87 [1.62 – 21.43]	2.54 [0.94 – 12.31]	–71.4	0.01

ROC analysis allows the comparison of the areas under the curve (AUCs) in order to identify the parameter with the best discrimination (Figure 6) and are summarized in Table 4 with their optimum sensitivity, specificity, and accuracy for each numerical parameter. The set of AUCs is significantly different from a random distribution (AUC of 0.5) at the alpha level of 0.026. Similar areas under the curve are observed around 0.79, as confirmed by the analysis

of variance with, whatever the loading, optimal thresholds giving the same sensitivities (87.5%), specificities (72.7%), and accuracy (81.5%) for all numerical outcomes. Comparable reduction was found for the best DXA parameters (ultra–distal aBMD) with an accuracy of 85.2% and an AUC of 0.77 (See appendix).

Table 4: For each numerical outcome, the area under the curve (AUC) with their sensitivity, specificity and accuracy of their optimal detection threshold

Parameters	AUC	Sensitivity (%)	Specificity (%)	Accuracy (%)
DXA Distal aBMD	0.773	81.8	87.5	85.2
Pistoia's Criterion				
Failure Load – axial	0.795	72.7	87.5	81.5
Failure Load – 75°	0.790	72.7	87.5	81.5
Failure Load – 45°	0.790	72.7	87.5	81.5
Failure Torque	0.790	72.7	87.5	81.5
Mohr–Coulomb's Criterion				
Failure Load – axial	0.795	72.7	87.5	81.5
Failure Load – 75°	0.801	72.7	87.5	81.5
Failure Load – 45°	0.790	72.7	87.5	81.5
Failure Torque	0.784	72.7	87.5	81.5

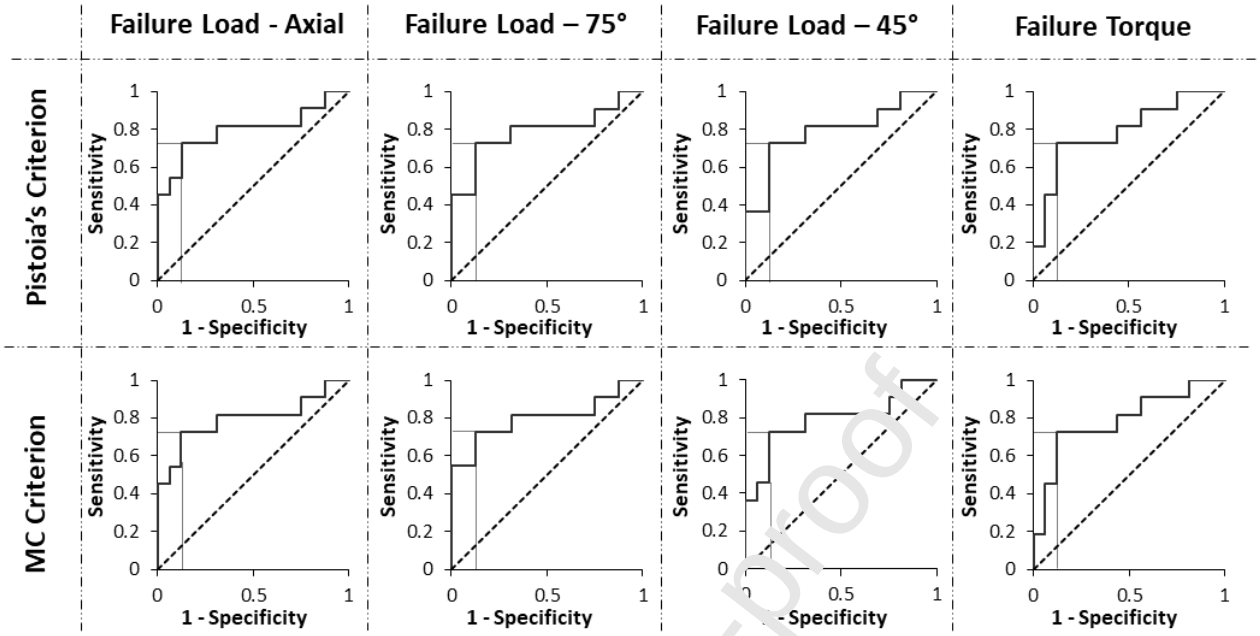

Figure 6: ROC curves (Sensitivity against 1 – Specificity) for the FE outcomes. The dotted lines indicate the best threshold detection. Similar results were observed regardless the loading condition or failure criteria.

4 Discussion

In this study, we investigated the sensitivity of loading conditions on μFE analysis provided by HR–pQCT for *ex vivo* radii fracture discrimination throughout a sensitivity/specificity study. Few studies have explored the influence of boundary conditions on radius bone strength. Troy and Grabiner demonstrated on a unique specimen that off–axis loads cause failure of the distal radius at lower magnitudes than axial loads [22]. The authors used homogenized finite element models of 10 cm of the radius based on standard computed tomography (CT) imaging (resolution of 0.455 x 0.455 x 1.25 mm/voxel), where material properties depended on the Hounsfield units (HU) of each voxel. Moreover, the authors used a local Mohr–Coulomb's failure criterion to determine numerical failure load. Another study [21] with similar modeling (CT imaging, continuum meshing, HU–based materials,

and local Mohr–Coulomb's failure criterion) on 22 specimens showed the influence of carpal bones on failure load. The authors found that scaphoid and lunate created stress concentration on the radius and resulted in a significantly lower (–49%) but highly correlated (R^2 = 0.93) fracture strength compared with an evenly distributed loading. These results, on 10 cm of the radius, indicated that boundary conditions had strong influence on the radius failure load, contrary to the current study on 1 cm. Indeed, our results showed that neither the loading conditions nor the failure criterion influence the fracture discrimination in the analysis. The strong correlation and linear relationships between the different failure load cases confirmed this observation with no change in the fracture bone classification. Even the loading orientation has few effects on the median, min, and max values throughout the axial and non-axial loading. Nevertheless, we can notice that, contrary to Troy and Grabiner who applied a non-axial force on their model [22], we applied a non-axial displacement. The choice to apply a displacement was motivated by the HR-pQCT standard μFE protocol which apply an axial displacement of 1% of the structure length. However, applying a displacement along an angle does not guarantee to get a resultant force along the same angle. The reaction forces we observed after the non-axial compression tests were indeed more axial than we expected. An average offset of 5° and 28° was observed between the applied displacement and reaction force (for the 75° case and 45° case respectively). The non-axial loading of the current study therefore corresponded to a 80° and 73° loadings. Even if these loadings are more axial than we expected, they were close to the most common angle of 75° observed during a fall [25]. The micro-structure of the restricted region of interest of 9.02 mm of radius thus seems to be much less sensitive to the loading orientation than the entire distal part of the bone (with

the articular surface and epiphysis) compared with a homogenized subject-specific finite element model [22].

It is important to note that these results are dependent on our samples which are limited to 27 bones. Nevertheless, μFE results consistently predict a lower strength (–42% to –72%) for the fractured group compared with that of non-fractured group and can be used to classify subjects with a distal radius fracture with an accuracy of 81.5% and an AUC of 0.79 and are strongly associated with fracture. Comparable reduction in the radius UD aBMD was found with an accuracy of 85.2% and an AUC of 0.77. Despite a sensitivity of 81.8% compared with the 72.7% of the FE outcomes, we cannot conclude that FE prediction is better or worse than that of the DXA parameters. Indeed, the comparison of the AUCs did not provide a significant difference between the curves. Similar results were found in a large cohort prospective study, where μFE derived parameters did not improve fractures predictions compared with ultra–distal radius DXA measurements [18]. Nevertheless, DXA measurements at the ultra-distal radius are rarely used for fracture prediction compared to femoral neck aBMD. The same study also showed that μFE analysis computed by HR–pQCT enhanced detection of incident fractures combined with femoral neck aBMD [18].

Some authors have investigated the influence of scanned areas in predicting bone strength [29,34,31,35,36]. These *in vitro* studies showed that a more distal area from the classic region improved the prediction of bone resistance (R^2 going from 0.79 to 0.94 [35] or from 0.73 to 0.76 with an R^2 of 0.78 for a full scanned bone [31]) and subsequently using two segments: the classic one combined with a more distal one in their following studies [37–40]. However, no data were provided with these two sections on the prediction of fractures

in vivo. Regarding the boundary conditions, it has been shown with a multiscale finite element analysis that simplified platen–compression boundary conditions alter cortical–trabecular load sharing at the distal radius [41,42]. Indeed, applying the same displacement on the entire distal surface may not represent the physiological conditions of a non–axial fall, which does not distribute the load uniformly over this distal surface. A previous study has introduced softer layers at the cut faces of the HR–pQCT's scanned section to obtain a more realistic load transfer to the scanned section [43]. This was achieved by comparing the calculated mean strain energy density in the clinical cross–sectional region with those calculated for the scanned region *in situ* determined from a full model of the distal radius. A stiffness of 15MPa was found to get a similar load transfer and distribution, which lead to axial and shear forces as well as torsion and bending moment, whereas axial loading through radio–carpal joint was considered. Moreover, the authors also showed that predicted forces and moments widely varied between subjects and depend on bone volume fraction, which means that physiological bone loading conditions on the cross–section were patient-specific [43]. Determination of realistic load transfer to the scanned region thus necessitate a full radius scanned region, which is not currently feasible *in vivo* with HR–pQCT. Nonetheless, it could be interesting to use the multiscale finite element model [41,42] under non-axial loading to obtain full bone FE modeling in order to observe the response to a more physiological nonaxial loading with softer layers at the cut face of the scanned section.

We made the choice in the current study to use only one Region of Interest (ROI) to reproduce our method *in vivo* with an acquisition time suitable for the patient. However, a larger scan region seems necessary to quantify physiological nonaxial loading to the

restricted HR–pQCT cross–sectional volume. A larger scan region may also allow us to observe sensitivity of the model due to its more complex structure, as in full distal radius hFE models [21,22,26]. The second version of the device, the XtremeCT II (Scanco Medical AG, Switzerland), offers a resolution of 61 μm and increases the ROI to 10.25 mm [8,44]. Its reduced acquisition time [38,45] could allow the possibility of studying loading sensitivity of subsequent ROI on patients but not yet on full bone. Finite element models with higher scanning regions should be developed in order to determine the effect of loading orientation on fracture detection.

5 Conclusions

The aim of the study was to assess if a change in loading conditions on μFE models based on HR–pQCT could improve fracture predictions. The study results suggested that changing the loading conditions (angle of the compression or torsion) in μFE models of 9.02 mm of the distal radius seems not to provide improvement in classifying *ex vivo* fractured and non-fractured radii from an elderly population. Improvements of FE models should be followed and might be obtained by enlarging the scanned region, which may influence fracture prediction [34,29,31,35]. A larger scanned region could be partially possible with the new version of the scanning equipment (XtremeCT II, Scanco Medical AG, Switzerland) having a lower scan time with a slightly higher ionizing dose [8,30,38]. Further study with a larger scan region of all distal radius should be investigated to identify if more realistic loadings could help in predicting osteoporosis fractures.

Acknowledgements

Conflict of interest

There is no conflict of interest for any of the authors.

Appendix

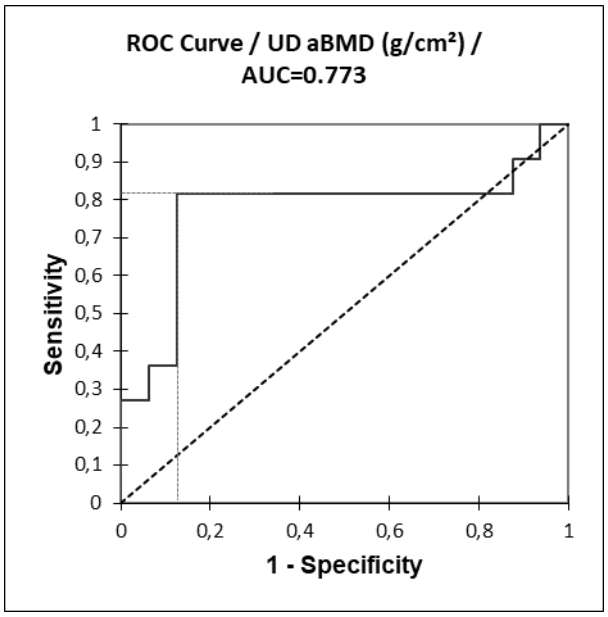

Appendix 1: ROC curves (Sensitivity against 1 – Specificity) for the DXA outcome. The dotted line indicates the best threshold detection.

References

[1] S. Khosla, E. Shane, A Crisis in the Treatment of Osteoporosis, J. Bone Miner. Res. Off. J. Am. Soc. Bone Miner. Res. 31 (2016) 1485–1487. https://doi.org/10.1002/jbmr.2888.

[2] C. Roux, K. Briot, Osteoporosis in 2017: Addressing the crisis in the treatment of osteoporosis, Nat. Rev. Rheumatol. 14 (2018) 67–68. https://doi.org/10.1038/nrrheum.2017.218.

[3] World Health Organization, Who scientific group on the assessment of osteoporosis at primary health care level, (2004).

[4] E.S. Siris, Y.-T. Chen, T.A. Abbott, E. Barrett-Connor, P.D. Miller, L.E. Wehren, M.L. Berger, Bone mineral density thresholds for pharmacological intervention to prevent fractures, Arch. Intern. Med. 164 (2004) 1108–1112. https://doi.org/10.1001/archinte.164.10.1108.

[5] S. Boutroy, M.L. Bouxsein, F. Munoz, P.D. Delmas, In vivo assessment of trabecular bone microarchitecture by high-resolution peripheral quantitative computed tomography, J. Clin. Endocrinol. Metab. 90 (2005) 6508–6515. https://doi.org/10.1210/jc.2005-1258.

[6] S. Boutroy, B. Van Rietbergen, E. Sornay-Rendu, F. Munoz, M.L. Bouxsein, P.D. Delmas, Finite element analysis based on in vivo HR-pQCT images of the distal radius is associated with wrist fracture in postmenopausal women, J. Bone Miner. Res. Off. J. Am. Soc. Bone Miner. Res. 23 (2008) 392–399. https://doi.org/10.1359/jbmr.071108.

[7] W. Pistoia, B. van Rietbergen, E.-M. Lochmüller, C.A. Lill, F. Eckstein, P. Rüegsegger, Estimation of distal radius failure load with micro-finite element analysis models based on three-dimensional peripheral quantitative computed tomography images, Bone. 30 (2002) 842–848. https://doi.org/10.1016/S8756-3282(02)00736-6.

[8] D.E. Whittier, S.K. Boyd, A.J. Burghardt, J. Paccou, A. Ghasem-Zadeh, R. Chapurlat, K. Engelke, M.L. Bouxsein, Guidelines for the assessment of bone density and microarchitecture in vivo using high-resolution peripheral quantitative computed tomography, Osteoporos. Int. J. Establ. Result Coop. Eur. Found. Osteoporos. Natl. Osteoporos. Found. USA. (2020). https://doi.org/10.1007/s00198-020-05438-5.

[9] B. van Rietbergen, K. Ito, A survey of micro-finite element analysis for clinical assessment of bone strength: the first decade, J. Biomech. 48 (2015) 832–841. https://doi.org/10.1016/j.jbiomech.2014.12.024.

[10] T. Chevalley, J.P. Bonjour, B. van Rietbergen, S. Ferrari, R. Rizzoli, Fracture history of healthy premenopausal women is associated with a reduction of cortical microstructural components at the distal radius, Bone. 55 (2013) 377–383. https://doi.org/10.1016/j.bone.2013.04.025.

[11] L.J. Melton, D. Christen, B.L. Riggs, S.J. Achenbach, R. Müller, G.H. van Lenthe, S. Amin, E.J. Atkinson, S. Khosla, Assessing forearm fracture risk in postmenopausal women, Osteoporos. Int. J. Establ. Result Coop. Eur. Found. Osteoporos. Natl. Osteoporos. Found. USA. 21 (2010) 1161–1169. https://doi.org/10.1007/s00198-009-1047-2.

[12] K.K. Nishiyama, H.M. Macdonald, D.A. Hanley, S.K. Boyd, Women with previous fragility fractures can be classified based on bone microarchitecture and finite element analysis measured with HR-pQCT, Osteoporos. Int. 24 (2013) 1733–1740. https://doi.org/10.1007/s00198-012-2160-1.

[13] N. Vilayphiou, S. Boutroy, P. Szulc, B. van Rietbergen, F. Munoz, P.D. Delmas, R. Chapurlat, Finite element analysis performed on radius and tibia HR-pQCT images and fragility fractures at all sites in men, J. Bone Miner. Res. 26 (2011) 965–973. https://doi.org/10.1002/jbmr.297.

[14] N. Vilayphiou, S. Boutroy, E. Sornay-Rendu, B. Van Rietbergen, F. Munoz, P.D. Delmas, R. Chapurlat, Finite element analysis performed on radius and tibia HR-pQCT images and fragility fractures at all sites in postmenopausal women, Bone. 46 (2010) 1030–1037. https://doi.org/10.1016/j.bone.2009.12.015.

[15] E. Biver, C. Durosier-Izart, T. Chevalley, B. van Rietbergen, R. Rizzoli, S. Ferrari, Evaluation of Radius Microstructure and Areal Bone Mineral Density Improves Fracture Prediction in Postmenopausal Women, J. Bone Miner. Res. Off. J. Am. Soc. Bone Miner. Res. 33 (2018) 328–337. https://doi.org/10.1002/jbmr.3299.

[16] C. Ohlsson, D. Sundh, A. Wallerek, M. Nilsson, M. Karlsson, N. Johansson, D. Mellström, M. Lorentzon, Cortical Bone Area Predicts Incident Fractures Independently of Areal Bone Mineral Density in Older Men, J. Clin. Endocrinol. Metab. 102 (2017) 516–524. https://doi.org/10.1210/jc.2016-3177.

[17] E. Sornay-Rendu, S. Boutroy, F. Duboeuf, R.D. Chapurlat, Bone Microarchitecture Assessed by HR-pQCT as Predictor of Fracture Risk in Postmenopausal Women: The OFELY Study, J. Bone Miner. Res. Off. J. Am. Soc. Bone Miner. Res. 32 (2017) 1243–1251. https://doi.org/10.1002/jbmr.3105.

[18] E.J. Samelson, K.E. Broe, H. Xu, L. Yang, S. Boyd, E. Biver, P. Szulc, J. Adachi, S. Amin, E. Atkinson, C. Berger, L. Burt, R. Chapurlat, T. Chevalley, S. Ferrari, D. Goltzman, D.A. Hanley, M.T. Hannan, S. Khosla, C.-T. Liu, M. Lorentzon, D. Mellstrom, B. Merle, M. Nethander, R. Rizzoli, E. Sornay-Rendu, B. Van Rietbergen, D. Sundh, A.K.O. Wong, C. Ohlsson, S. Demissie, D.P. Kiel, M.L. Bouxsein, Cortical and trabecular bone microarchitecture as an independent predictor of incident fracture risk in older women and men in the Bone Microarchitecture International Consortium (BoMIC): a prospective study, Lancet Diabetes Endocrinol. 7 (2019) 34–43. https://doi.org/10.1016/S2213-8587(18)30308-5.

[19] T.W. O'Neill, J. Varlow, A.J. Silman, J. Reeve, D.M. Reid, C. Todd, A.D. Woolf, Age and sex influences on fall characteristics, Ann. Rheum. Dis. 53 (1994) 773–775. https://doi.org/10.1136/ard.53.11.773.

[20] J. Oskam, J. Kingma, H.J. Klasen, Fracture of the distal forearm: epidemiological developments in the period 1971-1995, Injury. 29 (1998) 353–355. https://doi.org/10.1016/s0020-1383(97)00212-x.

[21] W.B. Edwards, K.L. Troy, Simulating distal radius fracture strength using biomechanical tests: a modeling study examining the influence of boundary conditions, J. Biomech. Eng. 133 (2011) 114501. https://doi.org/10.1115/1.4005428.

[22] K.L. Troy, M.D. Grabiner, Off-axis loads cause failure of the distal radius at lower magnitudes than axial loads: a finite element analysis, J. Biomech. 40 (2007) 1670–1675. https://doi.org/10.1016/j.jbiomech.2007.01.018.

[23] E. Zapata, F. Rongieras, J.-B. Pialat, H. Follet, D. Mitton, An ex vivo experiment to reproduce a forward fall leading to fractured and non-fractured radii, J. Biomech. 63 (2017) 174–178. https://doi.org/10.1016/j.jbiomech.2017.08.013.

[24] A. Laib, P. Rüegsegger, Comparison of structure extraction methods for in vivo trabecular bone measurements, Comput. Med. Imaging Graph. Off. J. Comput. Med. Imaging Soc. 23 (1999) 69–74. https://doi.org/10.1016/s0895-6111(98)00071-8.
[25] J. Chiu, S.N. Robinovitch, Prediction of upper extremity impact forces during falls on the outstretched hand, J. Biomech. 31 (1998) 1169–1176. https://doi.org/10.1016/S0021-9290(98)00137-7.
[26] W.B. Edwards, K.L. Troy, Finite element prediction of surface strain and fracture strength at the distal radius, Med. Eng. Phys. 34 (2012) 290–298. https://doi.org/10.1016/j.medengphy.2011.07.016.
[27] S.M.H. Kalajahi, S.M. Nazemi, J.D. Johnston, Separate modeling of cortical and trabecular bone offers little improvement in FE predictions of local structural stiffness at the proximal tibia, Comput. Methods Biomech. Biomed. Engin. 22 (2019) 1258–1268. https://doi.org/10.1080/10255842.2019.1661386.
[28] J.A. Macneil, S.K. Boyd, Bone strength at the distal radius can be estimated from high-resolution peripheral quantitative computed tomography and the finite element method, Bone. 42 (2008) 1203–1213. https://doi.org/10.1016/j.bone.2008.01.017.
[29] T.L. Mueller, M. Stauber, T. Kohler, F. Eckstein, R. Müller, G.H. van Lenthe, Non-invasive bone competence analysis by high-resolution pQCT: an in vitro reproducibility study on structural and mechanical properties at the human radius, Bone. 44 (2009) 364–371. https://doi.org/10.1016/j.bone.2008.10.045.
[30] D.E. Whittier, S.L. Manske, D.P. Kiel, M. Boyd-Boulerin, S.K. Boyd, Harmonizing finite element modelling for non-invasive strength estimation by high-resolution peripheral quantitative computed tomography, J. Biomech. 80 (2018) 63–71. https://doi.org/10.1016/j.jbiomech.2018.08.030.
[31] T.L. Mueller, D. Christen, S. Sandercott, S.K. Boyd, B. van Rietbergen, F. Eckstein, E.-M. Lochmüller, R. Müller, G.H. van Lenthe, Computational finite element bone mechanics accurately predicts mechanical competence in the human radius of an elderly population, Bone. 48 (2011) 1232–1238. https://doi.org/10.1016/j.bone.2011.02.022.
[32] P. Varga, S. Baumbach, D. Pahr, P.K. Zysset, Validation of an anatomy specific finite element model of Colles' fracture, J. Biomech. 42 (2009) 1726–1731. https://doi.org/10.1016/j.jbiomech.2009.04.017.
[33] S. Holm, A Simple Sequentially Rejective Multiple Test Procedure, Scand. J. Stat. 6 (1979) 65–70.
[34] T.L. Mueller, G.H. van Lenthe, M. Stauber, C. Gratzke, F. Eckstein, R. Müller, Regional, age and gender differences in architectural measures of bone quality and their correlation to bone mechanical competence in the human radius of an elderly population, Bone. 45 (2009) 882–891. https://doi.org/10.1016/j.bone.2009.06.031.
[35] P. Varga, D.H. Pahr, S. Baumbach, P.K. Zysset, HR-pQCT based FE analysis of the most distal radius section provides an improved prediction of Colles' fracture load in vitro, Bone. 47 (2010) 982–988. https://doi.org/10.1016/j.bone.2010.08.002.
[36] B. Zhou, Z. Zhang, Y. Hu, J. Wang, Y.E. Yu, S. Nawathe, K.K. Nishiyama, T.M. Keaveny, E. Shane, X.E. Guo, Regional Variations of HR-pQCT Morphological and Biomechanical Measurements of the Distal Radius and Tibia and Their Associations with Whole Bone Mechanical Properties, J. Biomech. Eng. (2019). https://doi.org/10.1115/1.4044175.
[37] P. Varga, E. Dall'Ara, D.H. Pahr, M. Pretterklieber, P.K. Zysset, Validation of an HR-pQCT-based homogenized finite element approach using mechanical testing of ultra-

distal radius sections, Biomech. Model. Mechanobiol. 10 (2011) 431–444. https://doi.org/10.1007/s10237-010-0245-3.

[38] H.S. Hosseini, A. Dünki, J. Fabech, M. Stauber, N. Vilayphiou, D. Pahr, M. Pretterklieber, J. Wandel, B. van Rietbergen, P.K. Zysset, Fast estimation of Colles' fracture load of the distal section of the radius by homogenized finite element analysis based on HR-pQCT, Bone. 97 (2017) 65–75. https://doi.org/10.1016/j.bone.2017.01.003.

[39] A.J. Arias-Moreno, H.S. Hosseini, M. Bevers, K. Ito, P. Zysset, B. van Rietbergen, Validation of distal radius failure load predictions by homogenized- and micro-finite element analyses based on second-generation high-resolution peripheral quantitative CT images, Osteoporos. Int. J. Establ. Result Coop. Eur. Found. Osteoporos. Natl. Osteoporos. Found. USA. 30 (2019) 1433–1443. https://doi.org/10.1007/s00198-019-04935-6.

[40] D. Schenk, A. Mathis, K. Lippuner, P. Zysset, In vivo repeatability of homogenized finite element analysis based on multiple HR-pQCT sections for assessment of distal radius and tibia strength, Bone. (2020) 115575. https://doi.org/10.1016/j.bone.2020.115575.

[41] J.E. Johnson, K.L. Troy, Simplified boundary conditions alter cortical-trabecular load sharing at the distal radius; A multiscale finite element analysis, J. Biomech. 66 (2018) 180–185. https://doi.org/10.1016/j.jbiomech.2017.10.036.

[42] J.E. Johnson, K.L. Troy, Validation of a new multiscale finite element analysis approach at the distal radius, Med. Eng. Phys. 44 (2017) 16–24. https://doi.org/10.1016/j.medengphy.2017.03.005.

[43] P. Christen, K. Ito, I. Knippels, R. Müller, G.H. van Lenthe, B. van Rietbergen, Subject-specific bone loading estimation in the human distal radius, J. Biomech. 46 (2013) 759–766. https://doi.org/10.1016/j.jbiomech.2012.11.016.

[44] D.E. Whittier, A.N. Mudryk, I.D. Vandergaag, L.A. Burt, S.K. Boyd, Optimizing HR-pQCT workflow: a comparison of bias and precision error for quantitative bone analysis, Osteoporos. Int. 31 (2020) 567–576. https://doi.org/10.1007/s00198-019-05214-0.

[45] S.L. Manske, E.M. Davison, L.A. Burt, D.A. Raymond, S.K. Boyd, The Estimation of Second-Generation HR-pQCT From First-Generation HR-pQCT Using In Vivo Cross-Calibration, J. Bone Miner. Res. Off. J. Am. Soc. Bone Miner. Res. 32 (2017) 1514–1524. https://doi.org/10.1002/jbmr.3128.

Highlights

- Experimental data on 27 *ex-vivo* radius are available. After a unique loading two groups were obtained: fractured and non-fractures radii.
- Axial or non-axial compression on HR-pQCT μFE models are associated with fragility fractures independently of DXA measurements.
- Loading orientations on a restricted area of 9.02 mm in HR-pQCT μFE models had few effects on failure loads or fracture prediction.